Advances in Applied Mathematics and Mechanics
Adv. Appl. Math. Mech., Vol. **1**, No. 4, pp. 481-509

DOI: 10.4208/aamm.09-m0915
August 2009

Numerical Study of Two-Winged Insect Hovering Flight

Yanjun Liu[1], Nansheng Liu[1,*] and Xiyun Lu[1]

[1] *Department of Modern Mechanics, University of Science and Technology of China, Hefei, Anhui 230026, China*

Received 15 January 2009; Accepted (in revised version) 15 April 2009
Available online 18 June 2009

Abstract. The two-winged insect hovering flight is investigated numerically using the lattice Boltzmann method (LBM). A virtual model of two elliptic foils with flapping motion is used to study the aerodynamic performance of the insect hovering flight with and without the effect of ground surface. Systematic studies have been carried out by changing some parameters of the wing kinematics, including the stroke amplitude, attack angle, and the Reynolds number for the insect hovering flight without ground effect, as well as the distance between the flapping foils and the ground surface when the ground effect is considered. The influence of the wing kinematic parameters and the effect of the ground surface on the unsteady forces and vortical structures are analyzed. The unsteady forces acting on the flapping foils are verified to be closely associated with the time evolution of the vortex structures, foil translational and rotational accelerations, and interaction between the flapping foils and the existed vortical flow. Typical unsteady mechanisms of lift production are identified by examining the vortical structures around the flapping foils. The results obtained in this study provide some physical insight into the understanding of the aerodynamics and flow structures for the insect hovering flight.

AMS subject classifications: 74F10, 74L15, 92C10, 76P05, 76D0, 76D17

Key words: Insect hovering flight, lattice Boltzmann method, ground effect, unsteady force, vortical structure.

1 Introduction

Insects flying through the air display superior maneuverability in their active flight in the complex environments, such as taking off backwards, flying sideways, and landing upside down [1, 2]. Such complex aerial feats are benefited from the unsteady and vortical flow induced by the wing flapping motion [3–6], which gives rise to the

*Corresponding author.
URL: `http://staff.ustc.edu.cn/~xlu/`
Email: liuyj1985@gmail.com (Y. J. Liu), lns@ustc.edu.cn (N. S. Liu), xlu@ustc.edu.cn (X. Y. Lu)

 ©2009 Global Science Press

high aerodynamic force needed for the insect flight. Typically, the wing stroke of an insect can be divided into four kinematic portions: two translational phases (upstroke and downstroke) when the wings sweep through the air with a high angle of attack, and two rotational phases (pronation and supination) when the wings rapidly rotate and reverse direction. How the flapping wings generate high aerodynamic lift for the insect hovering flight still is an important problem and is highly desired to be studied.

Several mechanisms about the enhanced production of the unsteady aerodynamic lift have been identified in the experimental studies, which are related to different stages of the wing flapping motion. A novel rotational mechanism, termed 'rotational lift', was found for the unsteady flow induced by the 'clap and fling' motion in the small insect flight [8–13]. During the fling phase of the 'clap and fling' motion, large attached leading edge vortices (LEVs) arise as the wings open up to form a V-shape by rotating around the trailing edges. The formation of LEVs is verified to result in a high lift production without the delay of Wagner effect [14,15]. In the translational phases, LEVs are also found attached to the leading edges when the wings move apart or towards each other at high attack angles. The stabilized LEVs are responsible for the large circulatory forces generated transiently in the upstroke and downstroke phases. This translational mechanism for high lift generation is called 'delayed stall' (or dynamic stall) [4,16]. Therefore, the existence of LEVs has been confirmed to be the most important aspect of the insect aerodynamics to generate significant lift on the flapping wings [17–22]. Another rotational mechanism is termed 'wake capture', which accounts for the large lift peak observed at the beginning of the stroke in case of advanced rotation, i.e., wing rotation preceding the stroke reversal [19]. It is suggested that the enhanced lift production in the insect hovering flight is due to the interaction of these three mechanisms occurring during the cyclic process of the two-winged flapping motion [16].

The unsteady mechanisms of the lift production in the insect hovering flight have also been investigated by numerical simulations [23–32]. Different wing kinematic modes have been employed to study the aerodynamic features in the insect hovering flight [25–37]. It is found that the wing kinematic parameters, such as the translational and rotational speeds, stroke amplitude, attack angle during the translational phases, are of appreciable effects on the lift production and the unsteady vortical flow [38–41]. Recently, Gao and Lu [42] first carried out the numerical simulations to study the ground effect on the unsteady forces and vortical structures around a flapping wing, and found that the ground effect plays an important role on the flight performance in the insect hovering flight. According to their study, three typical regimes of force behavior, i.e., force enhancement, force reduction, and force recovery regimes, are identified, depending on the distance between the flapping wing to the ground surface. To our knowledge, the aerodynamic forces and vortical flow evolution induced by the two-winged flapping motion are still not fully understood for the insect hovering flight, and the relevant studies are highly desired. We will thus investigate systematically the effects of the wing kinematic parameters and the ground effect on the unsteady aerodynamic mechanisms of the lift production in the two-winged insect

hovering flight.

In the present study, a 2D virtual model, which includes two elliptic foils with symmetric flapping motion, is used to deal with the effects of the wing kinematic parameters and the ground effect on the insect hovering flight. Although we recognize the limitation of this model, we nevertheless feel that it is reasonable to employ the 2D simulations to study the two-winged insect hovering flight. This consideration is confirmed by the experimental observations that even the 3D flow patterns are identified in insect flight [6], the spanwise flow within the vortex core is much weaker at low Reynolds number about 150 [5], and would not lead to the full separation of the LEVs for the amplitude-to-chord ratio between 3 and 5 [17, 18]. It is also confirmed that the unsteady forces predicted by the 2D computations agree well with the 3D experimental data [27] and the 3D computational results [29]. Thus, a 2D approach can be reasonably employed to predict the aerodynamic behaviors in the two-winged insect hovering flight. To deal with the unsteady forces and flow structures in the insect hovering flight, the 2D incompressible Navier-Stokes equations are solved using the lattice Boltzmann method (LBM), which can deal with the rigid wall condition [43] and determine the aerodynamic forces acting on the flapping wings conveniently [44].

This paper is organized as follows. The physical problem and mathematical formulation are described in Sec. 2. The numerical method and validation are given in Sec. 3. The effects of the wing kinematic parameters and the ground effect on the unsteady forces and vortical structures are discussed in Sec. 3. Finally, concluding remarks are given in Sec. 4.

2 Physical problem and mathematical formulation

To investigate the aerodynamic features in the two-winged insect hovering flight, the incompressible Navier-Stokes equations are used and given as

$$\frac{\partial \mathbf{u}}{\partial t} + \mathbf{u} \cdot \nabla \mathbf{u} = -\frac{1}{\rho} \nabla p + \nu \nabla^2 \mathbf{u}, \tag{2.1}$$

$$\nabla \cdot \mathbf{u} = 0, \tag{2.2}$$

where $\mathbf{u}$ is the velocity, p the pressure, ρ the density of the fluid, and ν the kinematic viscosity, respectively. To study the small insect flight, an idealized wing kinematic model was proposed by Miller and Peskin [31] to define the 'clap and fling' motion, which is a single wing stroke including only once upstroke, supination, and downstroke phase in sequence. Here, we extend this kinematic model to one full cycle of wing flapping motion and employ it to specify the kinematics of the two foils in Fig. 1. The kinematics of the left foil are described here. The right foil as it is applicable is the mirror image of the left foil during the flapping motion. As shown in Fig. 2, the translational phase is divided into three stages in sequence: the translational acceleration, the steady translation with a fixed velocity V and an attack angle α_m, and the translational deceleration. The translational velocities in the acceleration and deceleration

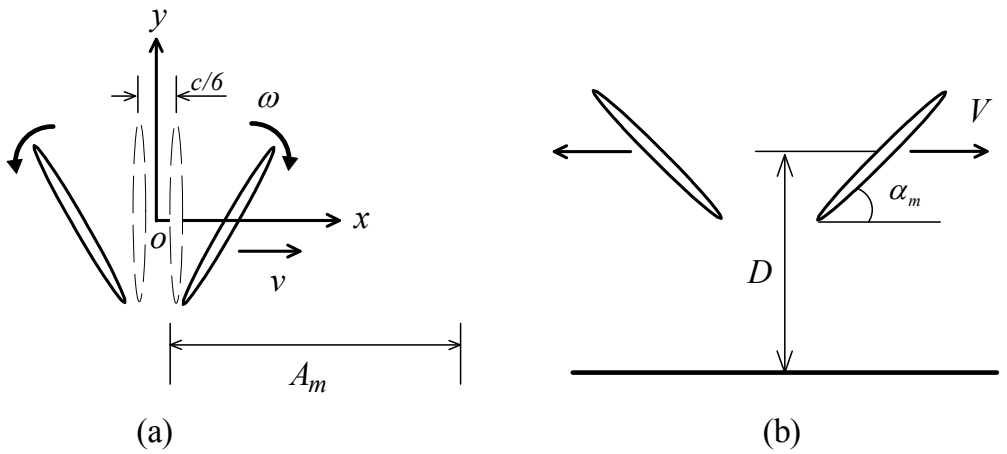

Figure 1: Sketch of the two-winged insect hovering flight without (a) and with ground effect (b).

stages are given as

$$v(\tau) = (-1)^{n+1}\frac{1}{2}V\{1-\cos[\frac{\pi(\tau-\tau_a)}{\Delta\tau_a}]\}, \quad \tau_a = \frac{n}{2}T, \tag{2.3}$$

and

$$v(\tau) = (-1)^{n+1}\frac{1}{2}V\{1+\cos[\frac{\pi(\tau-\tau_d)}{\Delta\tau_d}]\}, \quad \tau_d = \frac{n+1}{2}T-\Delta\tau_d, \tag{2.4}$$

respectively, where τ is the dimensionless time defined as $\tau{=}tV/c$, c is the chord length of the foil, n is an integer ($n \geq 0$), $\Delta\tau_a$ (or $\Delta\tau_d$) is the dimensionless duration of the translational acceleration (or deceleration), and T is the dimensionless duration of a full cycle of wing flapping motion defined as

$$T = 2(\Delta\tau_a + \Delta\tau_s + \Delta\tau_d), \tag{2.5}$$

where $\Delta\tau_s$ is the dimensionless duration of the steady translation. Therefore, the translation phase with $v(\tau){<}0$ denotes the downstroke motion for the left foil, and that with $v(\tau){>}0$ the upstroke motion. Here, $\Delta\tau_a$ and $\Delta\tau_d$ are taken to be 1.3, T is adjusted to obtain the stroke amplitude A_m desired by

$$A_m = \frac{1}{2}V(T-\Delta\tau_a-\Delta\tau_d), \tag{2.6}$$

During the rotational phase, the flapping foils rotate about the their centers. The angular velocity of the left wing during the rotational phase is given by

$$\omega(\tau) = (-1)^{n+1}\frac{1}{2}\Omega\{1-\cos[\frac{2\pi(\tau-\tau_r)}{\Delta\tau_r}]\}, \tag{2.7}$$

$$\tau_r = \frac{n}{2}T, \quad \text{or} \quad \frac{n}{2}T-\Delta\tau_r, \tag{2.8}$$

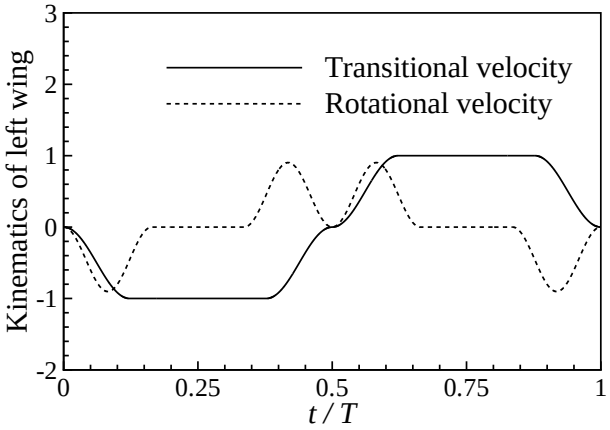

Figure 2: Kinematics of the left wing in one full cycle of flapping motion specified by the translational and rotational velocities.

where Ω is a constant obtained by $\Omega=(\pi-2\alpha_m)V/(\Delta\tau_r\, c)$, $\Delta\tau_r$ is the dimensionless duration of the rotational phase, which is set to be 1.74. Then, the rotational phase with $\omega(\tau)<0$ denotes the pronation motion for the left foil, and that with $\omega(\tau)>0$ the supination motion. Thus, the kinematics of the left wing in one full cycle of flapping motion is given by the time traces of the translational velocity v and rotational velocity ω depicted in Fig. 2. We use the chord length of the foil c and the steady translation velocity V as the length and velocity scales, respectively [31]. The Reynolds number is defined as $Re=Vc/\nu$. The corresponding non-dimensional variables shown in Eqs. (2.3)-(2.8) are still represented by the same symbols for writing convenience. To deal with the ground effect on the insect hovering flight, another parameter D is introduced to represent the distance between the flapping foils and the ground, or called the ground clearance [42, 45, 46]. In the present calculations, no-slip boundary condition is used on the flapping foils and the ground surface when present, and the boundary normal derivatives of velocity vanish in the far flow field. Initial flow field is set as rest for all the calculations.

3 Numerical method and validation

To solve Eqs. (2.1) and (2.2), the lattice Boltzmann equations with $D2Q9$ model are employed, which are proved to be second-order accuracy to recover the Navier-Stokes equations [47, 48], and given as

$$f_i(\mathbf{x}+\mathbf{e}_i\Delta t, t+\Delta t)-f_i(\mathbf{x},t)=-\frac{1}{\tau_{rt}}[f_i(\mathbf{x},t)-f_i^{eq}(\mathbf{x},t)], \tag{3.1}$$

where $f_i(\mathbf{x},t)$ is the distribution function for particles with velocity $\mathbf{e}_i$ at position $\mathbf{x}$ and time t, Δt is the time increment, and τ_{rt} is the relaxation time. The equilibrium

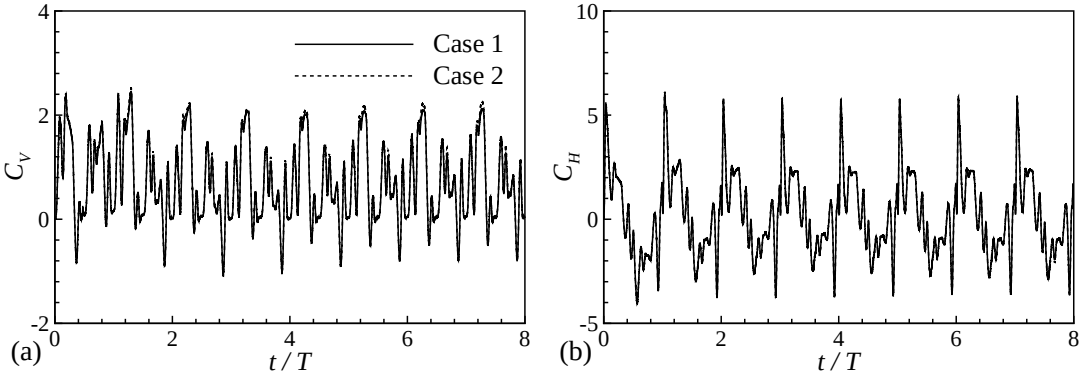

Figure 3: Time-dependent vertical (a) and horizontal (b) force coefficients of the left wing in the insect hovering flight without ground effect for A_m=4.0, α_m=45° and Re=100. Case 1: finest lattice spacing Δx=0.025 with the computational domain $[-10,10]\times[10,-20]$ in the x- and y-directions, respectively; Case 2: finest lattice spacing Δx=0.0125 with $[-20,20]\times[15,-30]$ in the x- and y-directions, respectively.

distribution function f_i^{eq} is defined as

$$f_i^{eq}=\omega_i\rho\Big[1+\frac{\mathbf{e}\cdot\mathbf{u}}{c_s^2}+\frac{\mathbf{uu}:(\mathbf{e}_i\mathbf{e}_i-c_s^2\mathbf{I})}{2c_s^4}\Big], \tag{3.2}$$

where ω_i is the weighing factor, c_s is the sound speed, ρ and $\mathbf{u}$ are the fluid density and velocity, respectively, which can be obtained by the distribution function,

$$\rho=\sum_i f_i,\quad \rho\mathbf{u}=\sum_i \mathbf{e}_i f_i. \tag{3.3}$$

To obtain the details of unsteady flow behaviors induced by the two-winged flapping motion, the grid refinement technique, i.e. the multi-block LBM [49,50], is employed to obtain fine grid resolution around the flapping foils. A bounce-back rule based on

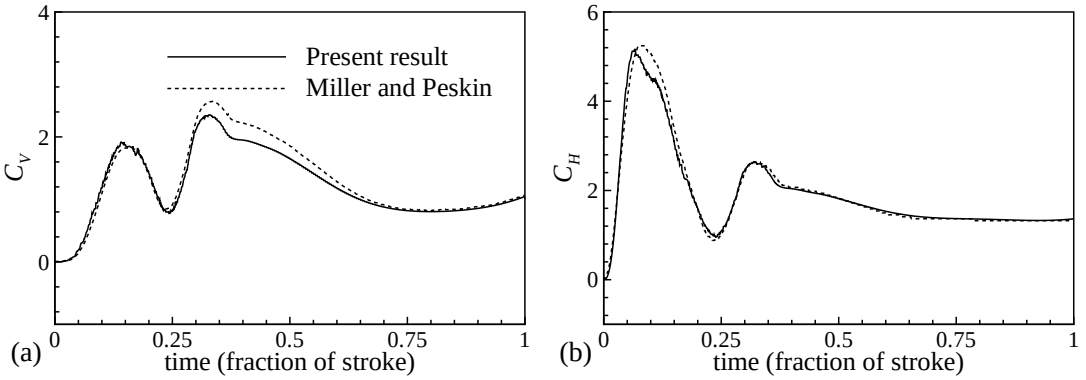

Figure 4: Validation of the present code and method by comparison of the vertical (a) and horizontal (b) force coefficients of the left wing induced by the 'single fling' motion for A_m=3.5, α_m=45° and Re=128.

the second-order accuracy interpolation [43] is employed to enforce the no-slip boundary condition on the flapping foils and the ground surface when present. Due to the wing flapping motion, some boundary nodes (computational nodes located within the moving foils) will change into fluid nodes (computational nodes located in the fluid flow field). In the present study, a second-order accuracy extrapolation strategy is used to define the distribution function right on such boundary nodes once they turns into the fluid nodes [51]. Since a 2D virtual mode is considered for the insect hovering flight, the vertical and horizontal force coefficients are used and defined as $C_V=F_V/(0.5\rho UV^2c)$ and $C_H=F_H/(0.5\rho UV^2c)$, respectively, where F_V and F_H are the vertical and horizontal forces acting on the flapping foils. Here, F_V and F_H are determined by use of the momentum-exchange method [44, 52]. The method to deal with the moving boundary and that to determine the aerodynamic forces were described in detail in the previous work referred above.

Here, to check the grid convergence, calculations by different lattice spacings were carried out for the unsteady flow induced by the two-winged flapping motion without ground effect. The time-dependent vertical and horizontal force coefficients for the left wing are typically shown in Fig. 3. It is seen that the results obtained by different computational conditions agree well with each other, indicating the independence of the lattice spacing and the computational domain size. Thus, the calculated results obtained by the computational conditions used in Case 2, i.e., finest lattice spacing Δx=0.0125 with a computational domain $[-20,20]\times[15,-30]$ in the $x-$ and $y-$ directions, respectively, are used to deal with the insect hovering flight without ground effect. Further, a typical flow induced by the one-winged 'single fling' motion studied extensively by Miller and Peskin [31] was calculated to validate the present code and method. In Fig. 4, the calculated time histories of the vertical and horizontal force coefficients are compared well with those obtained by Miller and Peskin [31]. Moreover, based on the extensive convergence studies (not shown here) and our previous work [42], the calculations to deal with the insect hovering flight under the ground effect are performed by used of the following computational conditions, finest lattice spacing Δx=0.0125 with a computational domain $[-20,20]\times[0,30]$ in the $x-$ and $y-$ directions, respectively.

4 Results and discussion

In this section, we present some typical results on the force behaviors and vortical structures of the two-winged insect hovering flight with and without ground effect. Based on the previous studies on modeling insect hovering flight [27, 28, 31, 42], the parameters used here are given as follows: the stroke amplitude A_m changes from 2.0 to 5.0, and the attack angle α_m from 30° to 60° [17,18]. The Reynolds number Re varies from 25 to 200, covering the range of Reynolds number in the small insect flight [8–13]. The thickness ratio of the foil is 0.04. As shown in Fig. 1, when the flapping wings follow the kinematics indicated in Fig. 2, a distance will be left between them when

they are in the parallel apposition together. This distance is set as $c/6$ in the present study. When the ground effect is considered, the ground clearance D ranges from 1 to 10. In the following subsections, the unsteady force behaviors of the left foil are discussed, the forces acting on the right foil are basically the mirror images of those on the left foil in the most calculations.

4.1 Effect of stroke amplitude A_m

The time evolution of vortical structures is closely associated with the aerodynamic feature in insect flight [17–22]. The unsteady lift production arises mainly from the interaction between the vortical structures (for example, the leading edge and trailing edge vortices) with the flapping foils [53, 54]. Here, as a typical case for the insect hovering flight without ground effect, the vortex evolution in one full cycle of wing flapping motion for A_m=4.0, α_m=45° and Re=100 is visualized in Fig. 5 and is discussed to understand the underlying mechanisms of lift production. Figs. 5(a)-5(d) show the vortical structures around the flapping foils during the wing downstroke phase from t/T=1/8 to 4/8. Large scale LEVs are formed mainly due to the wing pronation motion in Fig. 5(a), resulting in the high lift acting on the flapping foils by the 'rotational lift' mechanism [21, 31]. When these two foils are in the steady translation state, the LEVs remain attached to the flapping foils, contributing to the enhanced lift production in accordance with the 'delayed stall' mechanism [16]. At the end of the downstroke motion, the trailing edge vortices (TEVs) are shed from the flapping foils in Fig. 5(d). Figs. 5(e)-5(h) are the vorticity contours during the upstroke phase from t/T=5/8 to 8/8. After the translational acceleration of the upstroke phase, the foils move towards each other through the vortical wakes separated in the previous downstroke phase in Fig. 5(e). Meanwhile, new LEVs with opposite signs begin to grow and interact with those shed off in the previous downstroke phase. This vortex development is associated with the 'wake capture' mechanism of lift production [19]. In the steady translation stage of the upstroke phase in Fig. 5(f), the LEVs grow gradually and remain attached to the flapping foils. Due to the interaction of LEVs with the wake vortices and the growing TEVs, the lift production associated with the 'delayed stall' mechanism in the upstroke phase is expected to be relatively small. In Fig. 5(h), vortex shedding of the LEVs and TEVs is observed due to the translational deceleration. At the end of one cycle of wing flapping motion, two vortex pairs of TEVs shed from the flapping foils are drifted into the downwind flow, indicating a jetlike flow induced by the flapping motion of the insect wings [27].

To examine the effect of the stroke amplitude A_m on the insect hovering flight without ground effect, the time-averaged force coefficients $\bar{C}_V$ and $\bar{C}_H$ are discussed further. Based on our calculations, periodic variation of the time-dependent forces are achieved after about four cycles of wing stroke for all the calculations. The time-averaged values used below are obtained over several cycles of wing flapping motion in the periodic state. As suggested in the previous work [42], the absolute value of horizontal force is used when taking the average. The time-averaged force coefficients $\bar{C}_V$

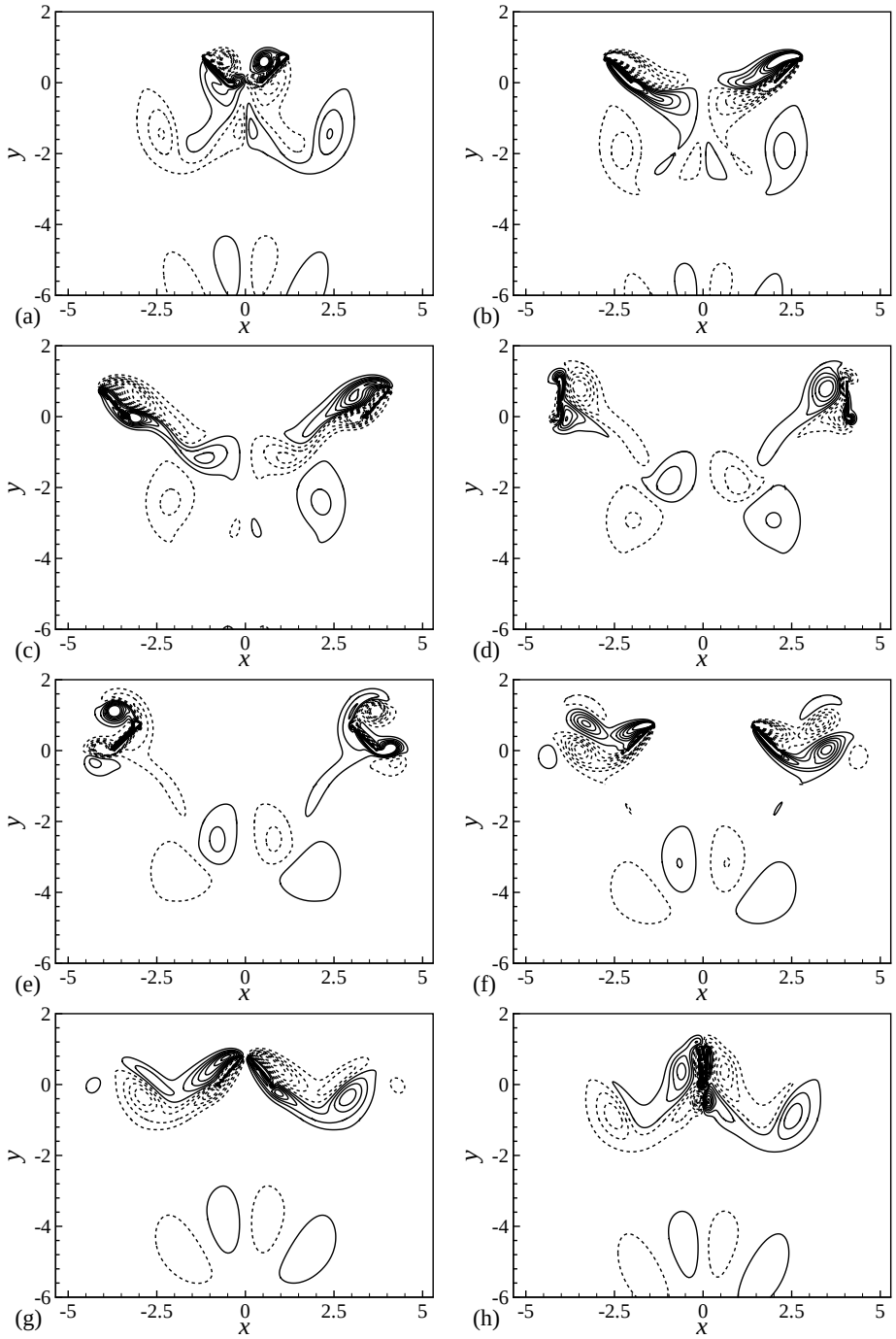

Figure 5: Vorticity contours during one full cycle of wing flapping motion without ground effect for A_m=4.0, α_m=45° and Re=100 at t/T =(a) 1/8, (b) 2/8, (c) 3/8, (d) 4/8, (e) 5/8, (f) 6/8, (g) 7/8 and (h) 8/8. Here, solid lines represent positive values (i.e, counterclockwise vortex) and dashed lines negative values (i.e., clockwise vortex). Increment of the contours is 1. The lines and increment used here are the same as ones shown in the following figures for all the vorticity plots.

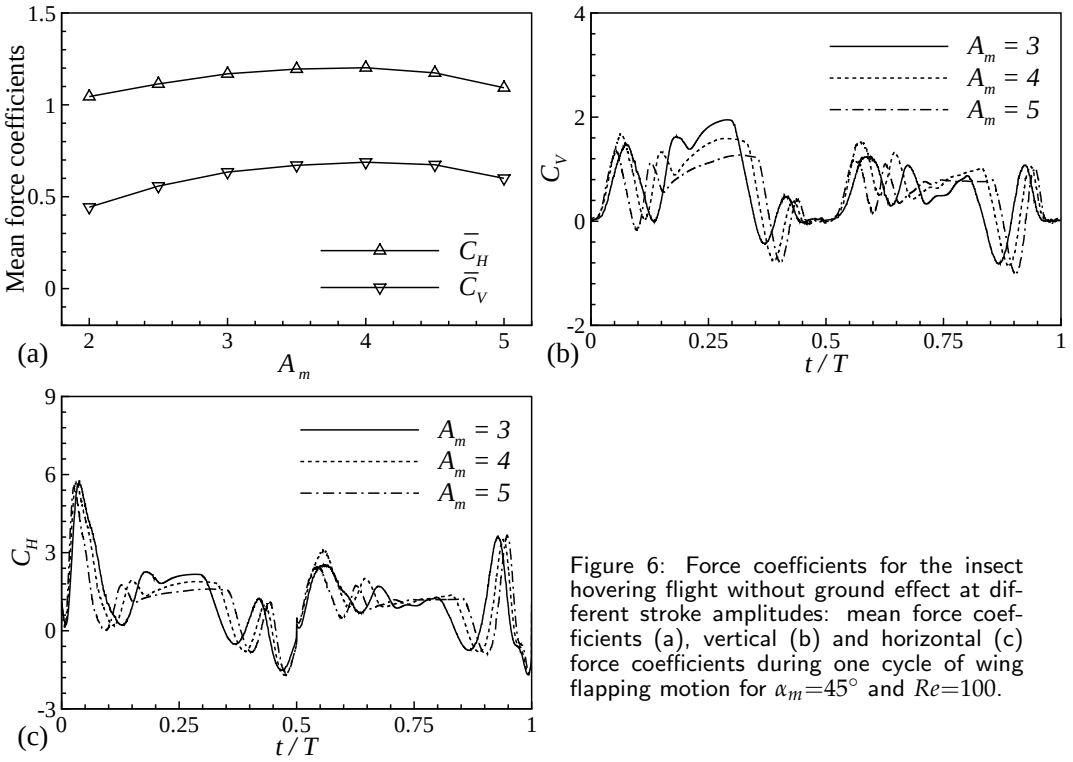

Figure 6: Force coefficients for the insect hovering flight without ground effect at different stroke amplitudes: mean force coefficients (a), vertical (b) and horizontal (c) force coefficients during one cycle of wing flapping motion for α_m=45° and Re=100.

and $\bar{C}_H$ versus the stroke amplitude A_m are shown in Fig. 6(a). With the increase of A_m from 2.0 to 4.0, the vertical and horizontal force coefficients increase slightly, and reach their maxima about A_m=4.0 with $\bar{C}_V$=0.69 and $\bar{C}_H$=1.20, respectively. The computational results are comparable to those obtained for the harmonic wing motion [27]. As A_m increases further to 5.0, $\bar{C}_V$ and $\bar{C}_H$ turn to decrease weakly. These behaviors of $\bar{C}_V$ and $\bar{C}_H$ are consistent with the experimental observation that the amplitude-to-chord ratio prefers to be in the range from 3.0 and 5.0 in small insect flight [17, 18].

For clearly exhibiting the force variation, the time-dependent force coefficients C_V and C_H over only one cycle of wing flapping motion after reaching the periodic state are shown in Figs. 6(b) and 6(c). Three typical stroke amplitudes A_m=3.0, 4.0 and 5.0 are considered here. In Fig. 6(b), the first peak of C_V occurs at t/T=0.065 approximately, corresponding to the rotational acceleration of the wing pronation motion that gives rise to the large attached LEVs resulting in high lift [31], as observed in Fig. 5(a). C_V approaches its second peak then drops to a platform distribution with relatively large value during the steady translation stage of the wing downstroke motion. This vertical force behavior contributes greatly to the lift production, as indicated in Figs. 5(b)-5(c). The third peak of C_V is small, occurring at t/T=0.42 approximately therefore corresponding to the supination motion of the wing downstroke phase. Another two peaks of C_V appear sequentially around t/T=0.58 and 0.65, as the consequences of the rotational and translational accelerations at the beginning of the wing upstroke mo-

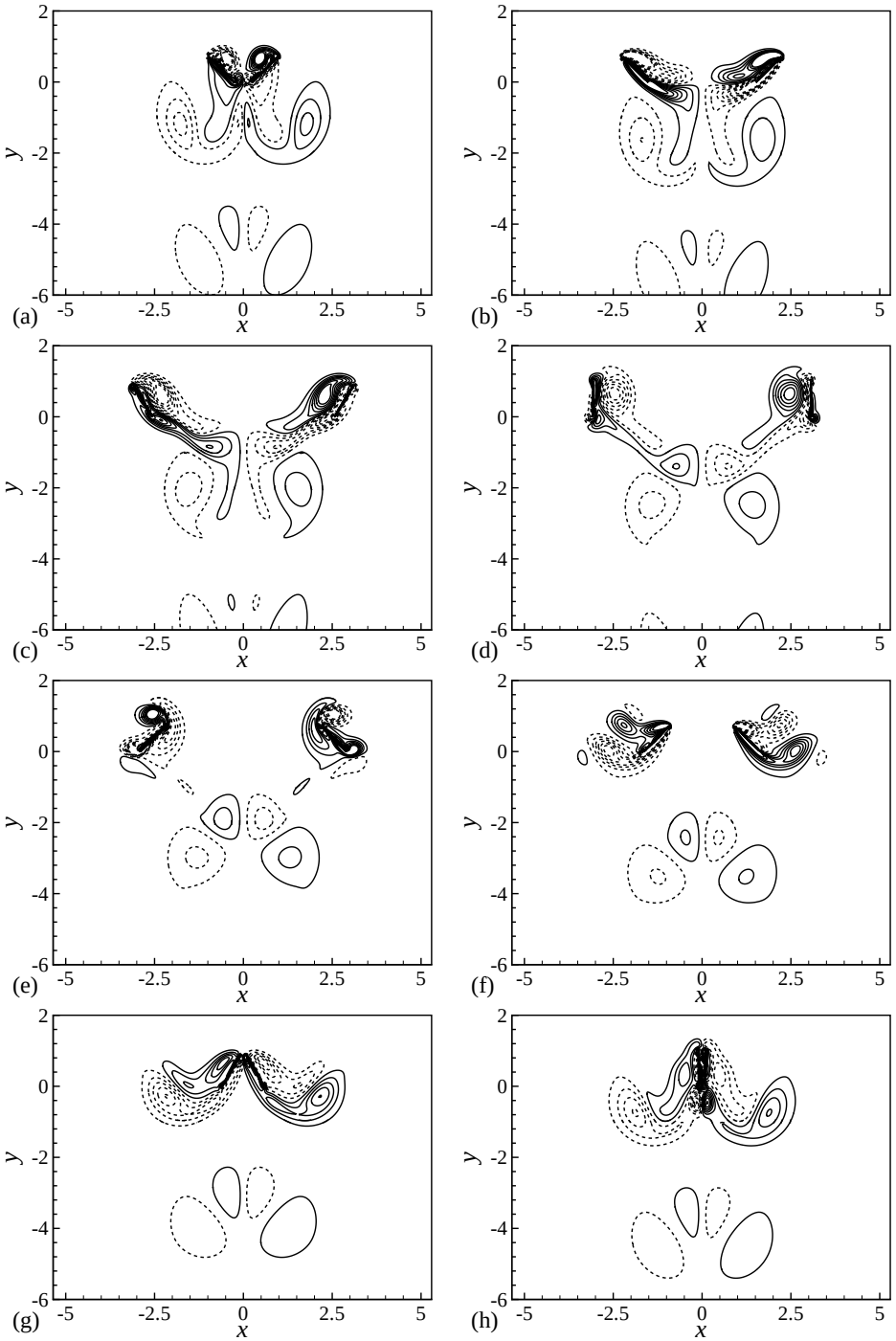

Figure 7: Vorticity contours during one full cycle of wing flapping motion without ground effect for A_m=3.0, α_m=45° and Re=100 at t/T=(a) 1/8, (b) 2/8, (c) 3/8, (d) 4/8, (e) 5/8, (f) 6/8, (g) 7/8 and (h) 8/8.

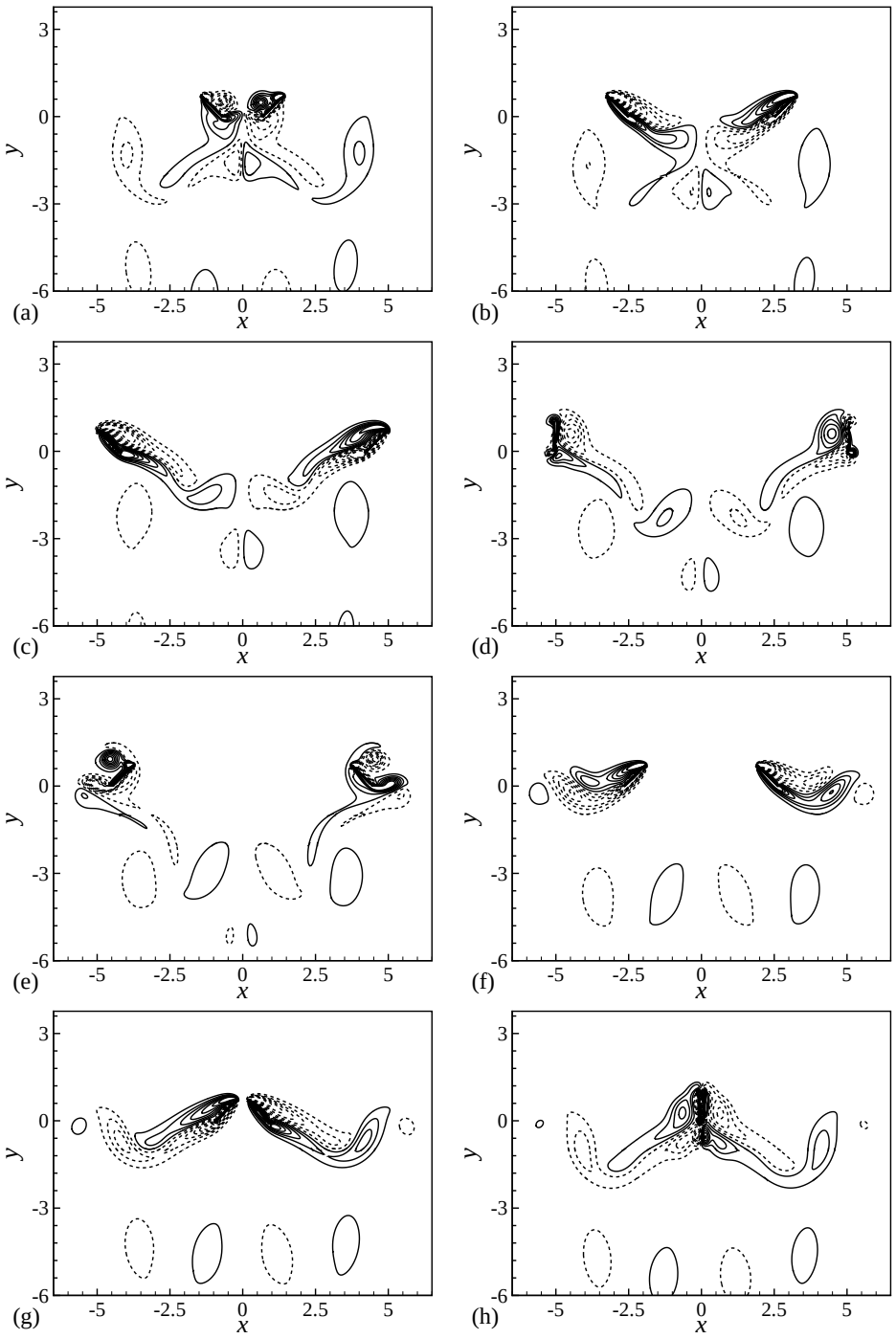

Figure 8: Vorticity contours during one full cycle of wing flapping motion without ground effect for A_m=5.0, α_m=45° and Re=100 at t/T =(a) 1/8, (b) 2/8, (c) 3/8, (d) 4/8, (e) 5/8, (f) 6/8, (g) 7/8 and (h) 8/8.

tion in Figs. 5(d)-5(e). During the steady translation stage of the wing upstroke phase, a platform distribution with nearly constant small C_V is observed, in accordance with the vortex evolution in Figs. 5(g)-5(h). This feature of lift force differs from that induced by the single stroke of 'clap and fling' wing motion [28,31], which presents a platform distribution of high lift coefficient during the 'fling' phase, since in that case the wings move toward each other through the undisturbed fluid [28,31]. The significant drop of C_V around t/T=0.87 corresponds to the translational deceleration of the wing upstroke phase. The last peak of C_V is presented at t/T=0.93 approximately, resulted from the rotational acceleration of the wing pronation motion at the end of upstroke phase. In Fig. 6(c), C_H reaches its first peak at t/T=0.03 approximately, due to the translational and rotational accelerations at the beginning of the wing downstroke motion. In sequence, the second small peak of C_H then its platform distribution with relatively steady values are observed during the steady translation stage of the downstroke motion. Due to the wing supination motion, another two peaks of C_H arise around t/T=0.42 and t/T=0.55, respectively. As the flapping wings move towards each other with fixed velocity V in the upstroke phase, C_H presents a small constant value. Then, C_H drops greatly due to the translational deceleration. In the late of the upstroke phase, the last peak value of C_H occurs at t/T=0.93 approximately, as the result of the wing pronation motion.

The weak dependence of $\bar{C}_V$ and $\bar{C}_H$ on A_m is also confirmed by the overview on Figs. 6(b) and 6(c), where little difference can be identified by integrating C_V or C_H over one full cycle of wing flapping motion for different A_m. As indicated in Figs. 7 and 8 for the vortical structures around the flapping foils, the time evolutions of vortical structures in one cycle of wing flapping motion for A_m=3.0 and 5.0 are quite similar to those for A_m=4.0 in Fig. 5. This visualization of vortex evolution is consistent with the time-dependent vertical and horizontal force behaviors predicted in Figs. 6(b) and 6(c).

4.2 Effect of attack angle α_m

The attack angle α_m during the steady translation stages of the wing flapping motion is an important parameter closely related to the vertical force [18]. Here, the effect of the attack angle α_m is investigated by examining the unsteady force behaviors and the time evolution of vortical structures around the flapping foils, with α_m ranging from 30° up to 60° for A_m=4.0 and Re=100. Fig. 9(a) shows the time-averaged force coefficients $\bar{C}_V$ and $\bar{C}_H$ versus the attack angle α_m. As measured in the previous experiments [17,18], the variation of α_m results in appreciable effect on the aerodynamic force behaviors. It is seen in Fig. 9(a) that $\bar{C}_H$ presents the considerable monotonic increase when α_m varies from 30° to 60°. Differently, $\bar{C}_V$ approaches to its maximum value 0.70 around α_m=50°, then decreases slightly when α_m increases further. This aerodynamic performance is basically consistent with the results of previous work [16,20].

To specify the effect of α_m on the unsteady forces, the time-dependent force coefficients C_V and C_H are typically shown in Figs. 9(b) and 9(c) for α_m=30°, 45° and 60°.

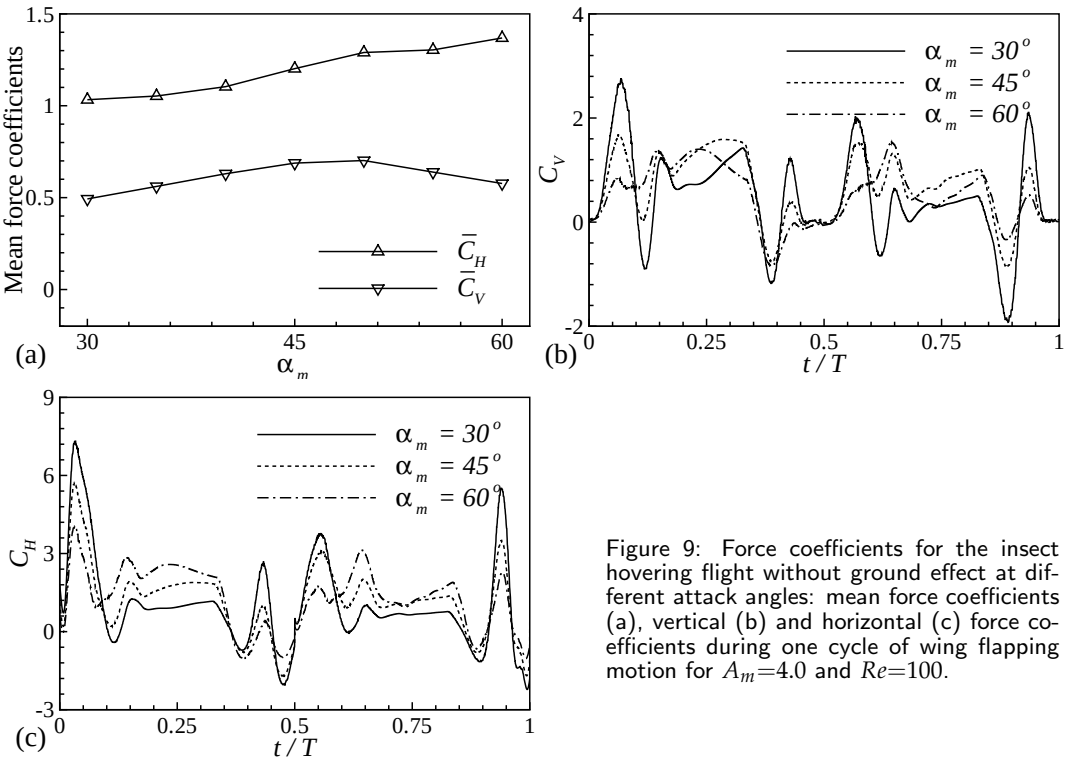

Figure 9: Force coefficients for the insect hovering flight without ground effect at different attack angles: mean force coefficients (a), vertical (b) and horizontal (c) force coefficients during one cycle of wing flapping motion for A_m=4.0 and Re=100.

In Fig. 9(b), the vertical force coefficients C_V for α_m=30° and 60° present the same time histories as that for α_m=45° in one cycle of wing flapping motion, which is described above in detail. The effect of α_m can be identified from the peak values of C_V associated with the wing pronation and supination motions, which decrease considerably with the increase of α_m from 30° to 60°, and from the platform distribution of C_V corresponding to the steady translation stages, which increase greatly as α_m varies up to 45° then drop appreciably when α_m increases further to 60°. This feature of C_V is responsible for the variation of $\bar{C}_V$ versus α_m depicted in Fig. 9(a). In Fig. 9(c), the peaks of C_H drops greatly during the wing pronation and supination motions when α_m varies from 30° to 60°. Different from the behavior of C_V in Fig. 9(b), the platform distribution of C_H increases monotonically with the increase of α_m from 30° to 60°. Considering the trends of $\bar{C}_V$ and $\bar{C}_H$ versus α_m in Fig. 9(a), the overview on Figs. 9(b)-9(c) reasonably leads to a conclusion that the aerodynamic features are mainly dominated by the unsteady force production associated with the steady translation stages.

To deal with the effect of α_m on the vortical structures, the vorticity contours for α_m=30° and 60° are shown in Figs. 10 and 11, respectively. The typical phenomena of vortical structures around the flapping foils can be identified in Figs. 10 and 11, such as the LEVs which are formed during the wing pronation motion and remain attached to the leading edges when the foils move apart during the downstroke phase,

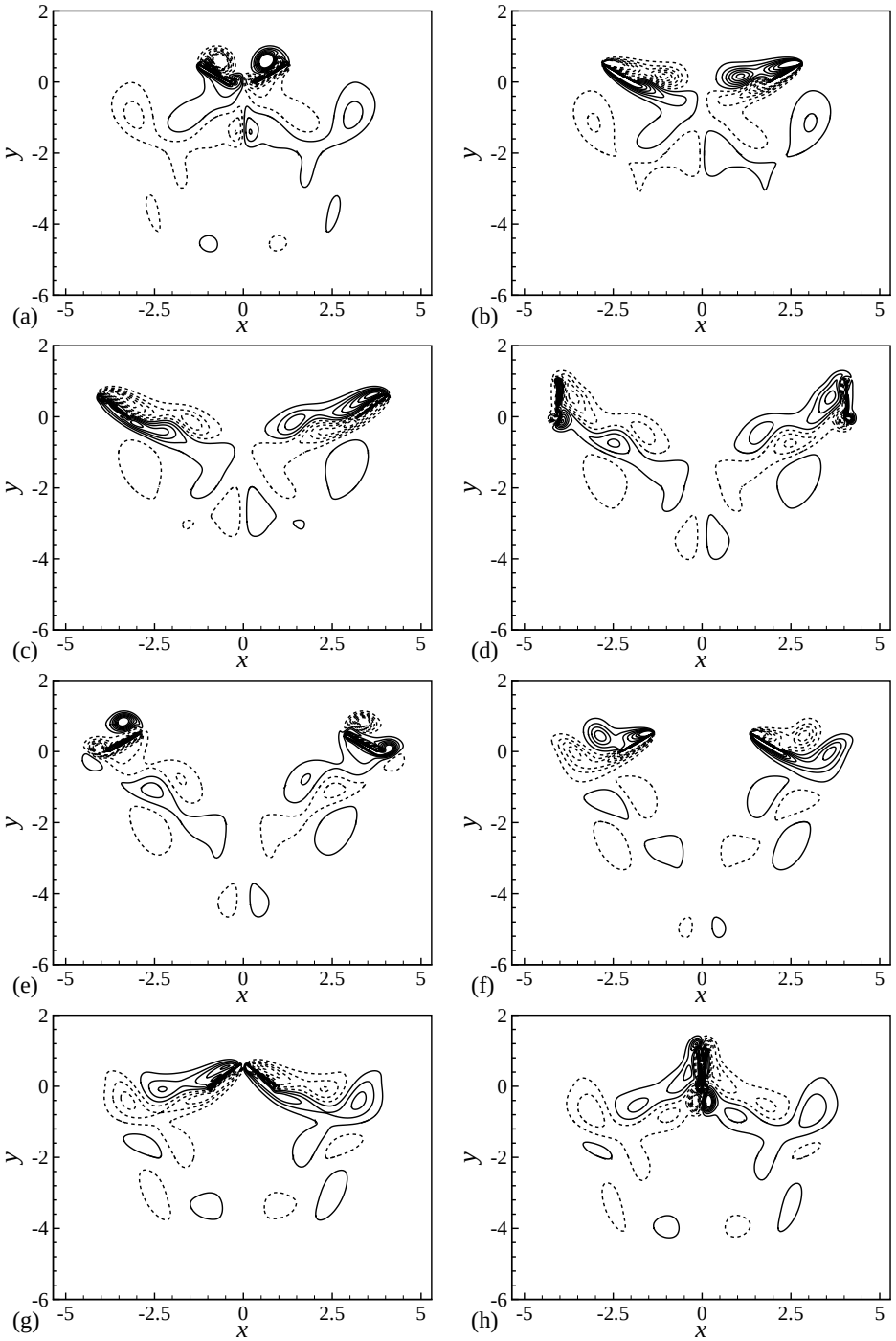

Figure 10: Vorticity contours during one full cycle of wing flapping motion without ground effect for A_m=4.0, α_m=30° and Re=100 at t/T =(a) 1/8, (b) 2/8, (c) 3/8, (d) 4/8, (e) 5/8, (f) 6/8, (g) 7/8 and (h) 8/8.

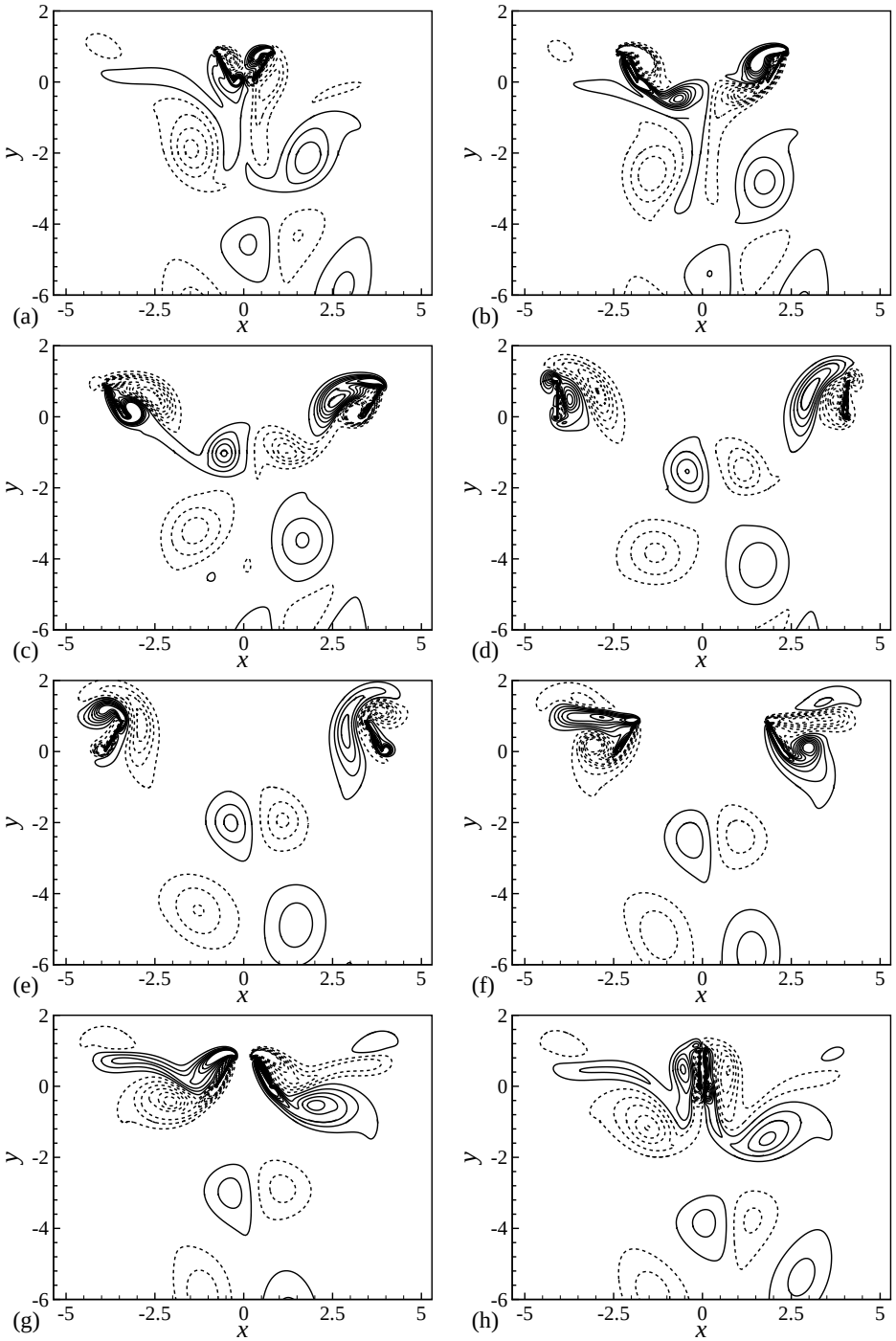

Figure 11: Vorticity contours during one full cycle of wing flapping motion without ground effect for A_m=4.0, α_m=60° and Re=100 at t/T =(a) 1/8, (b) 2/8, (c) 3/8, (d) 4/8, (e) 5/8, (f) 6/8, (g) 7/8 and (h) 8/8.

and the 'wake capture' process occurring due to the wing supination motion in the upstroke phase. In Fig. 10, the TEVs shed from the flapping foils do not drift away into the downwind evidently, indicating that the downward velocity of the jetlike flow induced by the flapping foils is trivial [27]. This feature of shedding TEVs is qualitatively consistent with the relatively small $\bar{C}_V$ for α_m=30° in Fig. 9(a). In Fig. 11, weak asymmetry of vortical structures is observed around the flapping foils, in particular during the wing pronation motion. According to the dynamics of vortical flow, this feature of vortex evolution is expected to break the symmetry of the unsteady forces acting on the left and right foils, which consequently leads to the instability in the insect hovering flight.

4.3 Effect of Reynolds number *Re*

We further discuss the effect of Reynolds number *Re* on the force behaviors and vortical structures in the insect hovering flight. Here, the Reynolds number varies from 25 to 200, and the stroke amplitude and attack angle are fixed at A_m=4.0 and α_m=45°, respectively. In Fig. 12(a), the time-averaged vertical and horizontal force coefficients, $\bar{C}_V$ and $\bar{C}_H$, are shown versus the Reynolds number *Re*. It is indicated that the variation of Reynolds number have a little influence on the time-averaged vertical force coefficient $\bar{C}_V$, which increases weakly to its maximum about 0.73 as *Re* changes from 25 up to 175, and decreases slightly when *Re* increases further to 200. Differently, the

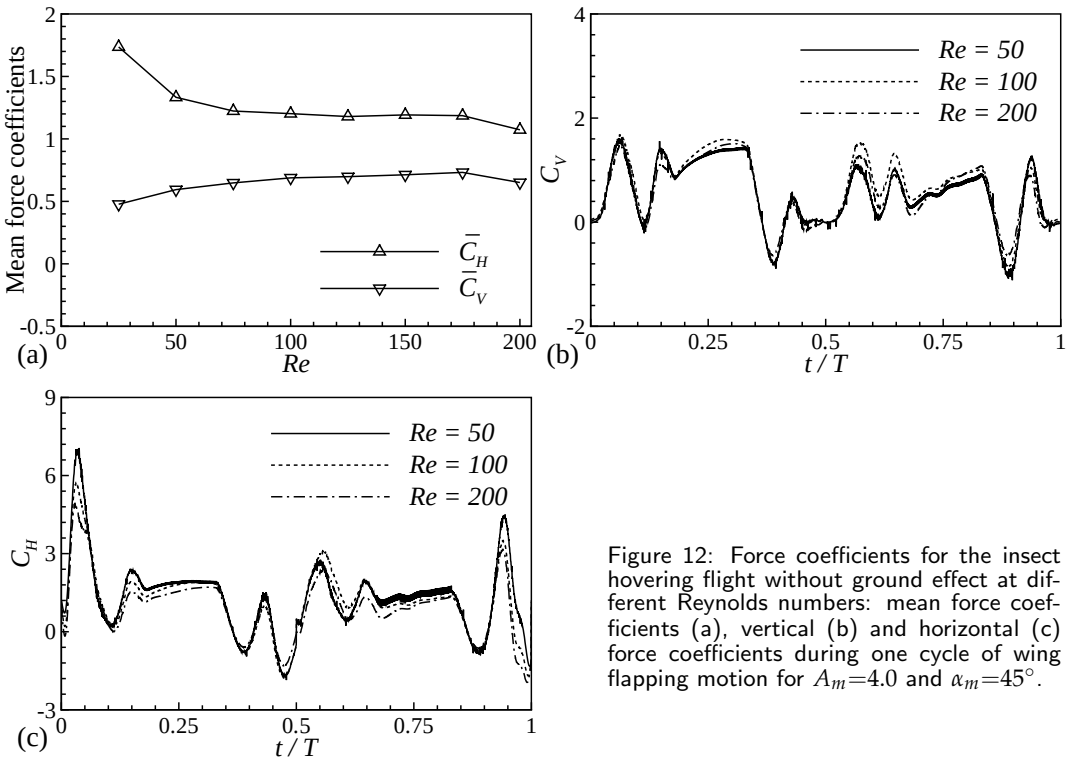

Figure 12: Force coefficients for the insect hovering flight without ground effect at different Reynolds numbers: mean force coefficients (a), vertical (b) and horizontal (c) force coefficients during one cycle of wing flapping motion for A_m=4.0 and α_m=45°.

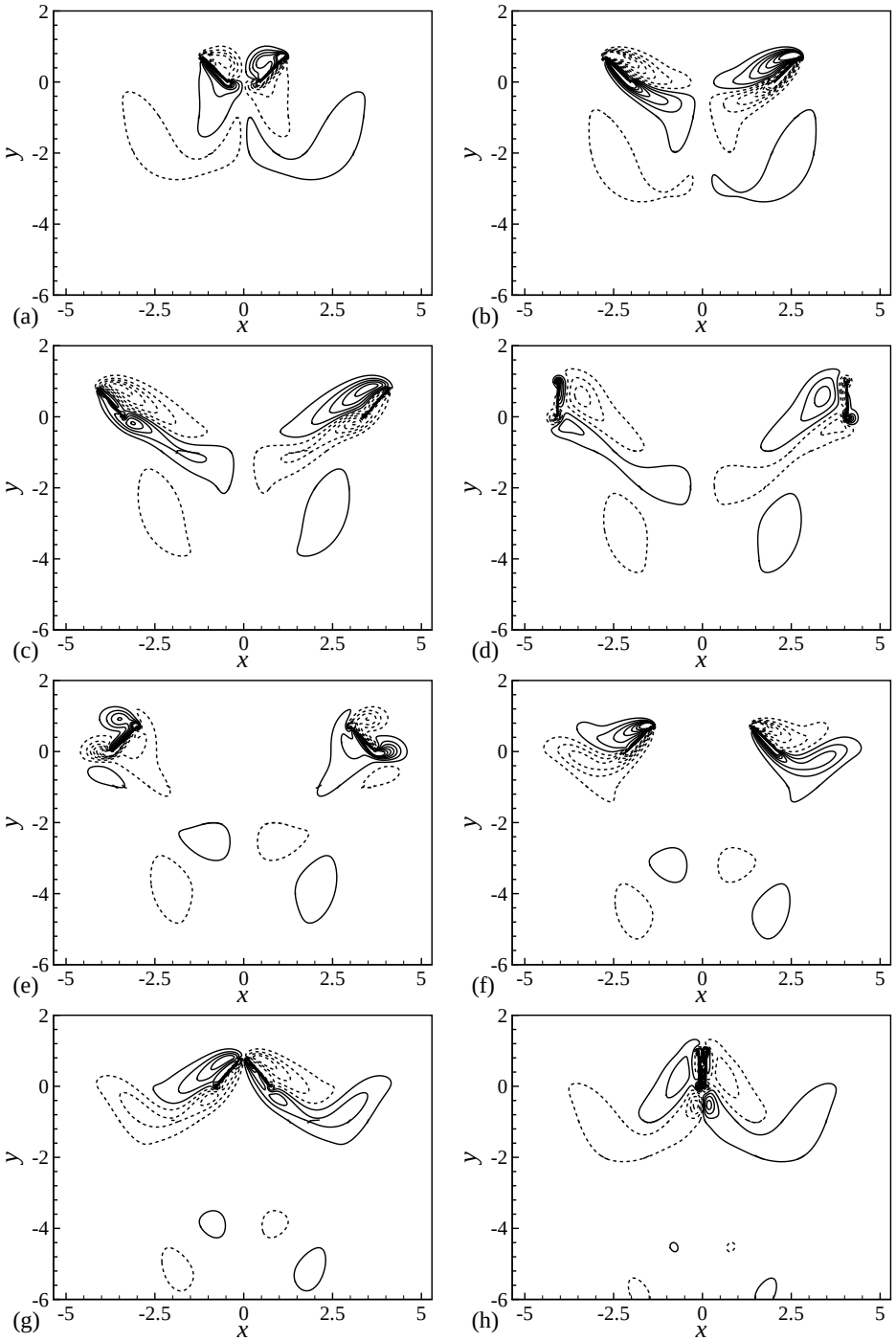

Figure 13: Vorticity contours during one full cycle of wing flapping motion without ground effect for A_m=4.0, α_m=45° and Re=50 at t/T=(a) 1/8, (b) 2/8, (c) 3/8, (d) 4/8, (e) 5/8, (f) 6/8, (g) 7/8 and (h) 8/8.

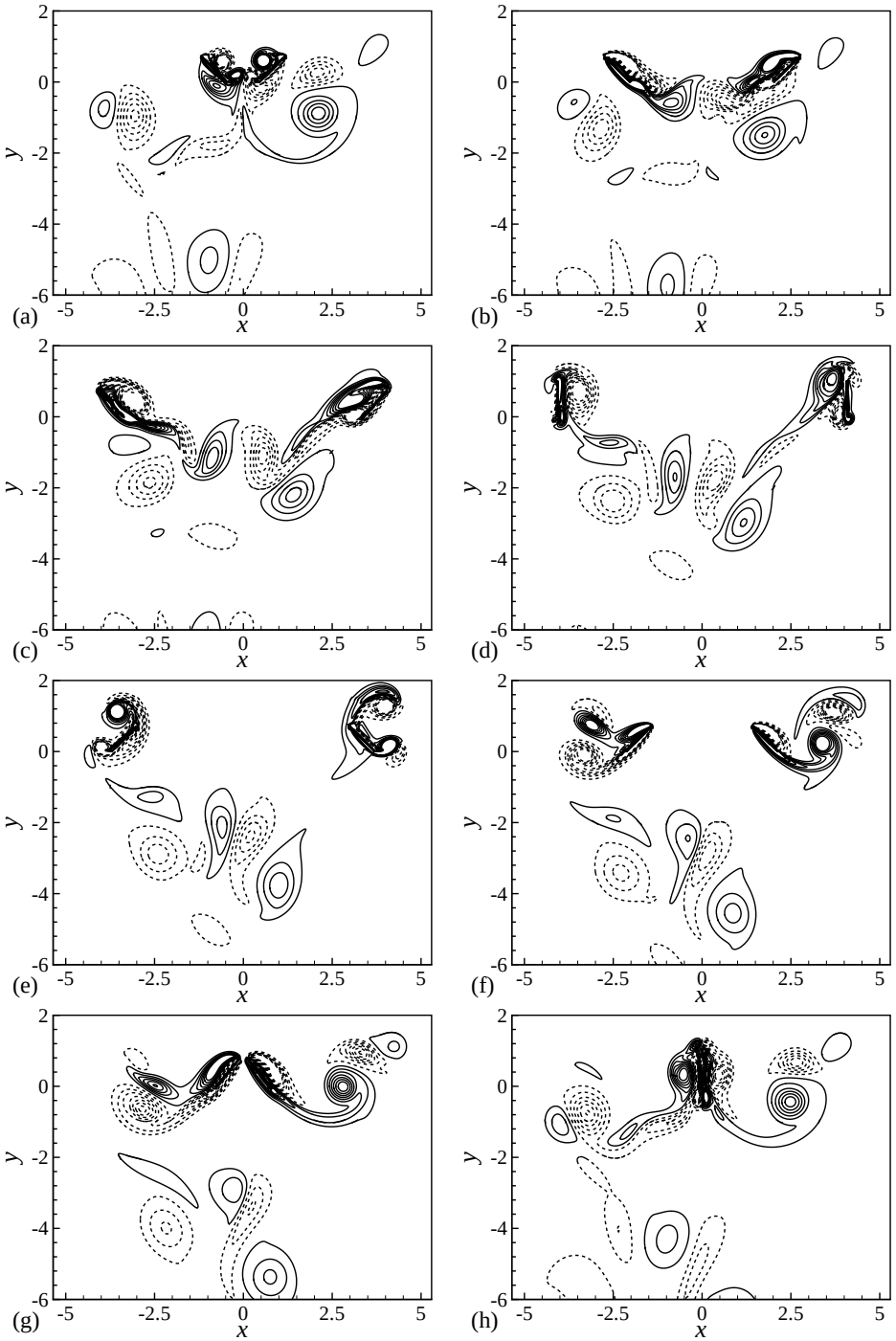

Figure 14: Vorticity contours during one full cycle of wing flapping motion without ground effect for A_m=4.0, α_m=45° and Re=200 at t/T =(a) 1/8, (b) 2/8, (c) 3/8, (d) 4/8, (e) 5/8, (f) 6/8, (g) 7/8 and (h) 8/8.

effect of Re on the time-averaged horizontal force coefficient is more remarkable in Fig. 12(a). $\bar{C}_H$ presents a high value about 1.73 at low Reynolds number Re=25, and drops greatly to about 1.20 as Re increases to 75. In the range $75 \leq Re \leq 175$, $\bar{C}_H$ remains nearly a constant value, indicating the weak dependence of $\bar{C}_H$ on the Reynolds number. When Re increases up to 200, $\bar{C}_H$ decrease considerably to a value about 1.05. This behavior of $\bar{C}_H$ is basically in agreement with the experimental measurements [21].

In Figs. 12(b) and 12(c), the time-dependent force coefficients C_V and C_H are typically shown for Re=50, 100 and 200 to examine in detail the force behaviors. In Fig. 12(b), the peak values of C_V corresponding to the wing pronation and supination motions, as well as the platform distribution of C_V related to the steady translation stages in the downstroke and upstroke phases, increase weakly when Re increase from 50 to 100, then decrease slightly as Re varies up to 200. This behavior of C_V in response to the variation of Re is consistent with the weak influence of Re on $\bar{C}_V$ indicated in Fig. 12(a). Basically, C_H in Fig. 12(c) drops with the increase of Re, in accordance with the behavior of $\bar{C}_H$ shown in Fig. 12(a). The trend of C_V versus Re is different from that induced by the single stroke of 'clap and fling' motion, which decrease greatly with the increase of Re. [28, 31] This difference of C_V in response to the increase of Re should mainly arise from the interaction of the flapping wings with the vortical structures separated in the previous cycles of wing flapping motion.

To examine the effect of Re on the time evolution of vortical structures, the vorticity contours for Re=50 and 200 are shown in Figs. 13 and 14, respectively. Similar to the vortical structures in Fig. 5, symmetrical vortex development is observed in Fig. 13 for low Reynolds number Re=50. The relevant mechanisms of unsteady forces have been well discussed in the previous subsections. Fig. 14 shows the vorticity contours during one cycle of wing flapping motion for Re=200. Obviously, strong vortex asymmetry is visualized from the time evolution of vortical structures, in particular by examining the TEVs shed into the downwind flow from the flapping foils. The symmetry break of the vortical structures should be due to the nonlinear dynamics of vortical flow for high Reynolds number, as reported by the numerical study of Lu and Liao. [33] The asymmetry of vortical structures for Re=200 are expected to lead to the instability in the insect hovering flight. This finding of vortex development for high Reynolds number is consistent with the fact that the 'clap and fling' motion is mainly employed by small insects, with the Reynolds number no more than 150 [8–13].

4.4 Effect of ground clearance D

The ground effect is verified to play an important role on the unsteady forces induced by the one-winged flapping motion [42]. Here, calculations are carried out to deal with the ground effect on the aerodynamic forces and vortical structures induced by the two-winged flapping motion, with the clearance D varying from 1 to 10, and the other computational parameters fixed at A_m=4.0, α_m=45° and Re=100.

We first discuss the ground effect on the force behaviors. Fig. 15(a) shows the time-averaged force coefficients $\bar{C}_V$ and $\bar{C}_H$ versus the ground clearance D. When the

flapping foils are close to the ground surface, i.e. D=1, $\bar{C}_V$ and $\bar{C}_H$ are greatly enhanced. This force behaviors are also observed in the our previous work [42]. The force coefficients $\bar{C}_V$ and $\bar{C}_H$ present the monotonic trends with the increase of D, decreasing gradually to the corresponding values without ground effect when D increases to 10. Here, to be recalled that $\bar{C}_V$ and $\bar{C}_H$ without ground effect have been obtained in Fig. 6(a), which are about 0.69 and 1.20, respectively. Different from the force behaviors induced by the one-winged flapping motion [42], no force reduction regime is identified in the present calculations. These trends of force behaviors induced by the two-winged flapping motion should be resulted from the difference of the kinematics of the flapping foils and the wing-wing interaction between the flapping foils [21].

In Figs. 15(b) and 15(c), the time-dependent force coefficients C_V and C_H are shown for typical ground clearances D=1, 4 and 8, to examine the detail force behaviors under the influence of the ground surface. When the ground clearance is small (D=1), it is indicated in Fig. 15(b) that the great enhancement of $\bar{C}_V$ in Fig. 15(a) is mainly due to three augmented contributions of C_V in one cycle of wing flapping motion. One is the first peak of C_V linked to the wing rotational acceleration at the beginning of the downstroke phase, which is greatly augmented for the small ground clearance. The other two come from the peaks of C_V around t/T=0.16 and 0.68, which are enhanced so greatly that the sequent platform distributions of C_V in the steady translation stages disappear. Therefore, for a small ground clearance, e.g. D=1, the platform distributions of C_V associated with the 'delayed stall' mechanism are no longer the major contributions to the lift production. As the ground clearance D increases to 8, the ground

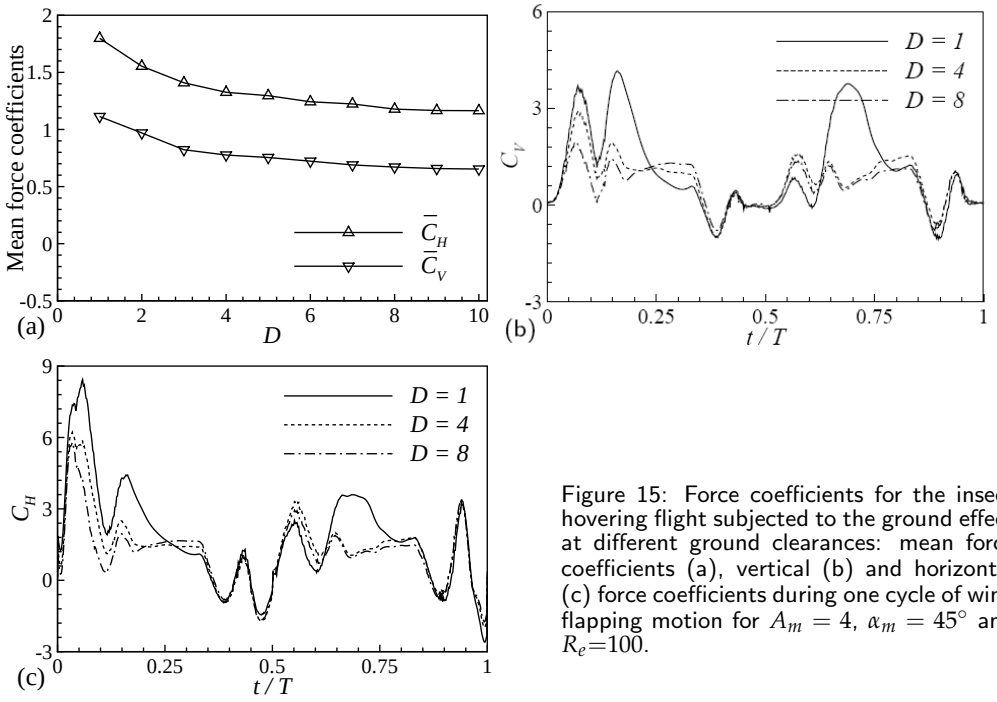

Figure 15: Force coefficients for the insect hovering flight subjected to the ground effect at different ground clearances: mean force coefficients (a), vertical (b) and horizontal (c) force coefficients during one cycle of wing flapping motion for $A_m = 4$, $\alpha_m = 45^\circ$ and R_e=100.

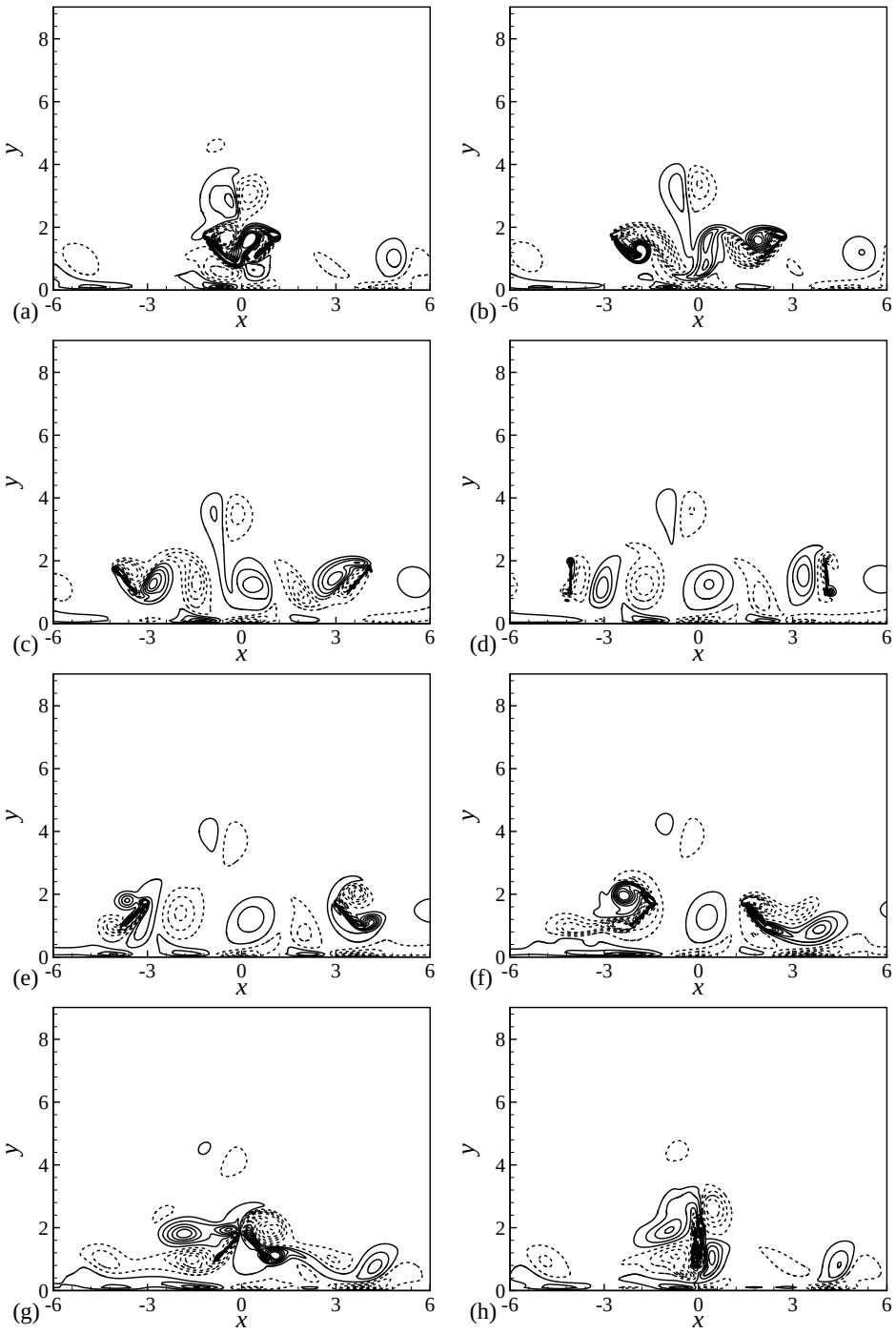

Figure 16: Vorticity contours during one full cycle of wing flapping motion subjected to the ground effect for A_m=4.0, α_m=45°, Re=100 and D=1.0 at t/T =(a) 1/8, (b) 2/8, (c) 3/8, (d) 4/8, (e) 5/8, (f) 6/8, (g) 7/8 and (h) 8/8.

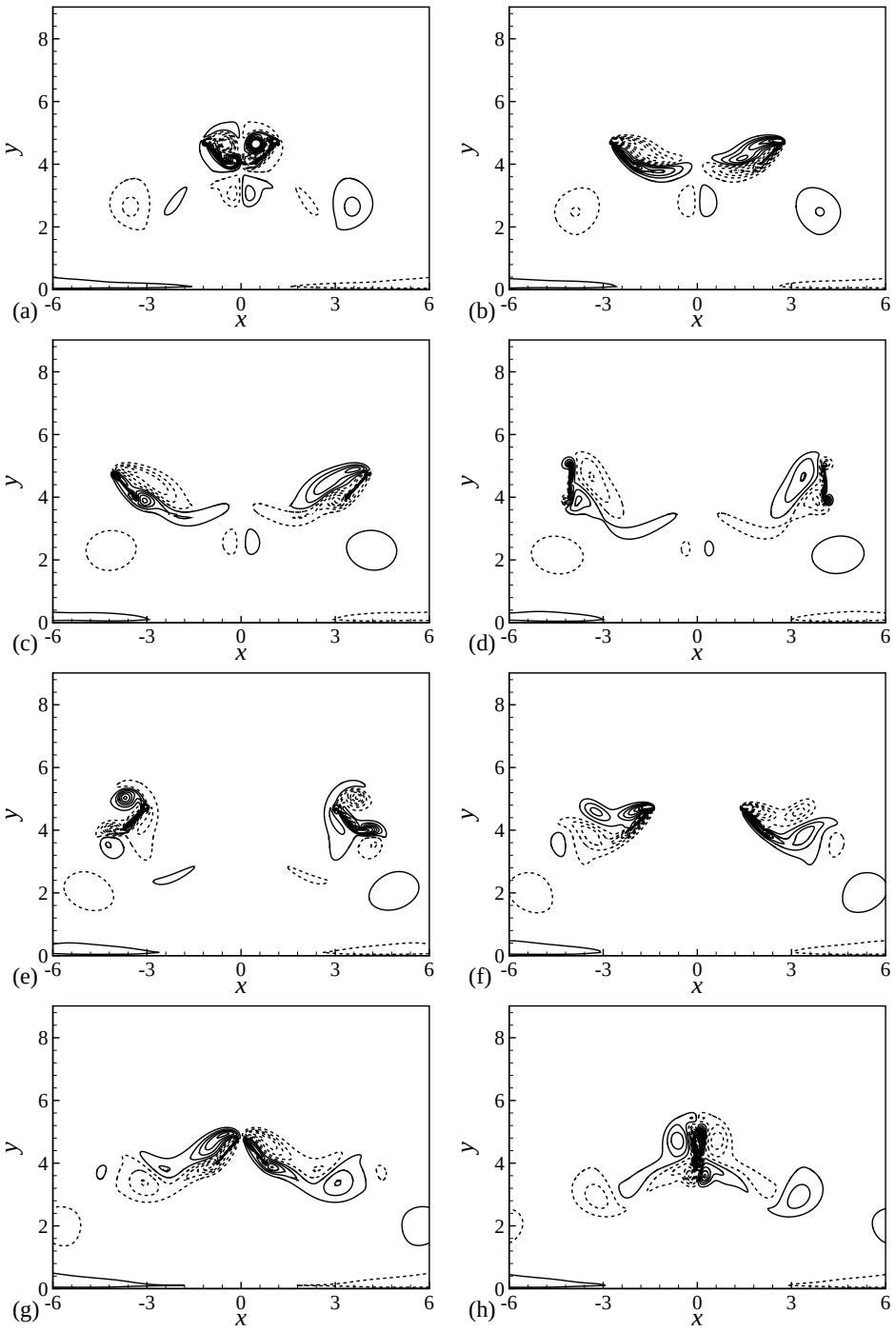

Figure 17: Vorticity contours during one full cycle of wing flapping motion subjected to the ground effect for A_m=4.0, α_m=45°, Re=100 and D=4.0 at t/T =(a) 1/8, (b) 2/8, (c) 3/8, (d) 4/8, (e) 5/8, (f) 6/8, (g) 7/8 and (h) 8/8.

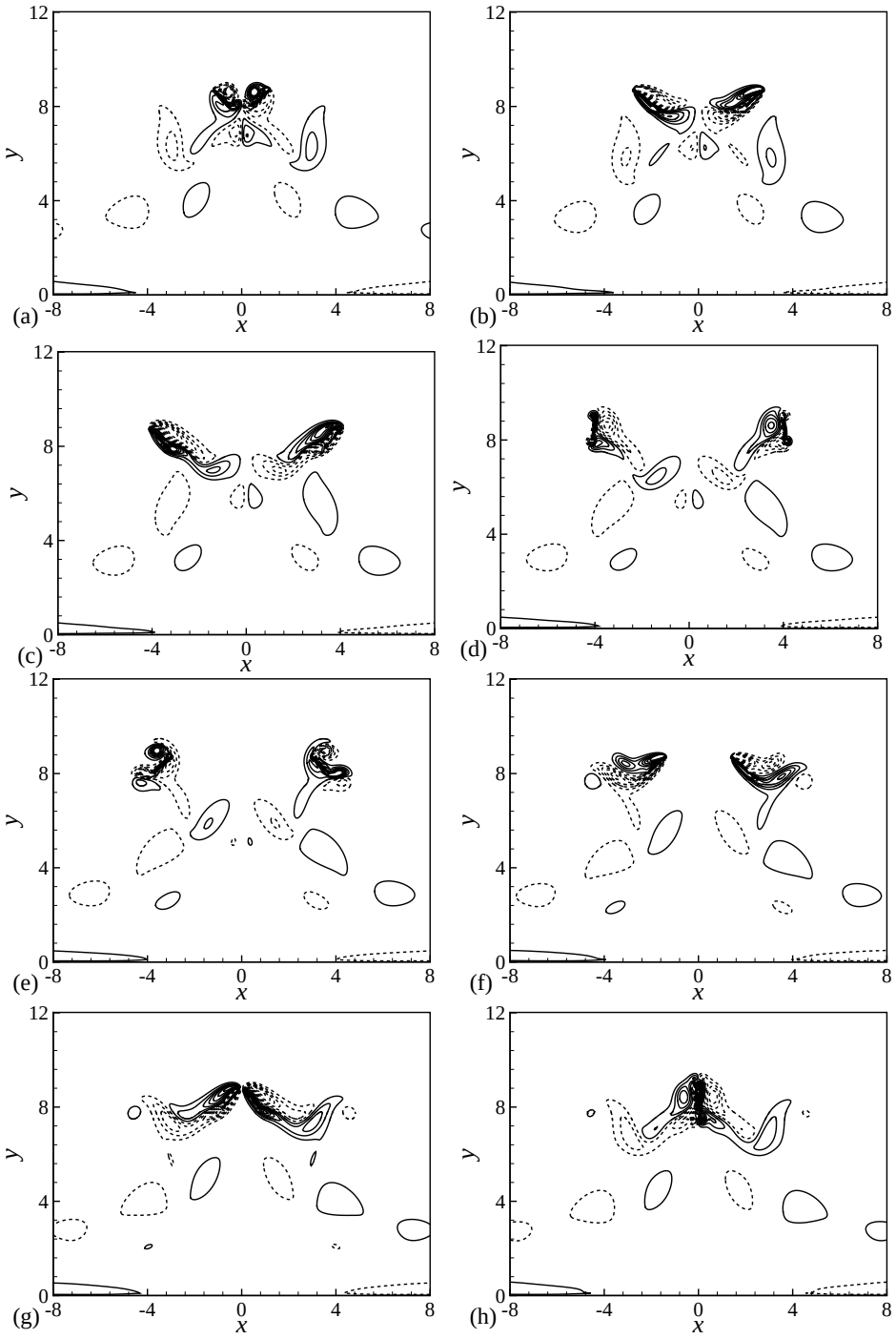

Figure 18: Vorticity contours during one full cycle of wing flapping motion subjected to the ground effect for A_m=4.0, α_m=45°, Re=100 and D=8.0 at t/T =(a) 1/8, (b) 2/8, (c) 3/8, (d) 4/8, (e) 5/8, (f) 6/8, (g) 7/8 and (h) 8/8.

effect on C_V is damped quickly and C_V presents the same time-dependent behavior as that without ground effect, consistent with trend of $\bar{C}_V$ shown in Fig. 15(a). Similar to the response of C_V to the ground effect for $D = 1$, the first peak of C_H linked to the wing rotational acceleration at the beginning of the downstroke phase, together with the peaks of C_H related to the steady translation stages during the downstroke and upstroke phases, are remarkably augmented. This feature of C_H is responsible for the great enhancement of $\bar{C}_H$ at small ground clearance in Fig. 15(a). With the increase of D up to 8, the ground effect becomes weak and C_H quickly recovers the time-dependent behavior without ground effect.

Here, the time evolution of vortical structures around the flapping foils is discussed for D=1 to understand the effect of ground surface. Figs. 16(a)-16(d) shows the vorticity contours during the downstroke phase. Compared to the vortex development without ground effect shown above, the vortical structures become more complicated when the ground surface present. During the wing pronation motion of the downstroke phase, large scale LEVs are formed and attached to the flapping foils in Fig. 16(a), contributing to the first high peaks of C_V (Fig. 15(b)) and C_H (Fig. 15(c)). Meanwhile, the TEVs are shed from the flapping foils to form a relative strong vortex pair close to the trailing edge, with the positive vortex under the right foil in Fig. 16(a). Due to the ground effect, this vortex pair gives rise to another vortex pair right on the ground surface. According the dynamics of vortical flow, the jetlike downwind flow induced by these two vortex pairs is of benefit to the enhanced force production in the following steady translation stage, and should be responsible for the high peaks of C_V (Fig. 15(b)) and C_H (Fig. 15(c)) at t/T=0.16 approximately. When the flapping foils move apart, large scale LEVs and TEVs are shed off alternatively, as shown in Figs. 16(c)-16(d). During the upstroke phase in Figs. 16(e)-16(h), the flapping foils move towards each other through the vortical structures shed off in the previous downstroke phase. The strong 'wake capture' process is visualized in Fig. 16(e) at the beginning of the upstroke phase, which is responsible for the peaks of C_V (Fig. 15(b)) and C_H (Fig. 15(c)) about t/T=0.68. During the upstroke phase, strong interaction between the flapping foils and ground surface can be identified by the elongated vortical structures right on the ground surface in Figs. 16(f)-16(g). In Fig. 16, weak vortex asymmetry is observed over one cycle of wing flapping motion, indicating the consequent weak instability in the insect hovering flight subjected to the effect of small ground clearance.

In Figs. 17 and 18, the vortical structures for the ground clearances D=4 and 8 are shown over one cycle of wing flapping motion. With D increases over 4, the effect of ground surface on the vortical structures around the flapping foils becomes weak, the symmetrical vortex development is observed in Figs. 17 and 18, similar to the typical vortex evolution without ground effect, as shown in Fig. 5. Due to the presence of ground surface, the TEVs shed from the flapping foils are swept horizontally in the downwind flow. This influence of ground surface on the vortical structures is also observed in our previous work to study the one-winged flapping motion under the ground effect [42].

5 Conclusions

We have investigated the two-winged insect hovering flight by extensive calculations using the lattice Boltzmann method (LBM). By examing the unsteady forces and vortical structures, the effects of wing kinematic parameters, including the stroke amplitude, attack angle, and Reynolds number, as well as the ground effect, are studied to provide physical understanding of the aerodynamic performance in the insect hovering flight. Here, we briefly summary the results obtained in the present study and discuss the underlying mechanisms of the insect hovering flight with and without ground effect.

By examining in detail the time evolution of vortical structures around the flapping foils without ground effect, typical unsteady mechanisms of high lift production, including 'rotational lift', 'delayed stall', and 'wake capture', are identified during one cycle of wing flapping motion. Based on the systematic parameter studies, the force characteristics are verified to be closely associated with vortical structures, foil translational and rotational accelerations, and interaction between the flapping foil and the existing vortical flow. Basically, the present results are qualitatively consistent with the experimental observation of small insect flight. The time-averaged vertical and horizontal forces are found to be weakly dependent on the stroke amplitude as it varies from 3.0 to 5.0, corresponding to the range of amplitude-to-chord ratio employed in the small insect flight. By checking the effect of attack angle, the maximum of lift force is obtained for the attack angle 45°. It is found that the unsteady forces associated with the steady translation stages are dominant to the flight performance. Weak dependence of aerodynamic performance is identified for Reynolds number in the range from 50 to 100. For high Reynolds number, strong vortex asymmetry is visualized by examining the vortical structures, which indicates the flight instability for small insect flight. When the ground effect is considered, the aerodynamic forces are significantly enhanced for small ground clearance. As the ground clearance increases, the unsteady force quickly recover their behaviors without ground effect.

The results obtained in this study are helpful to understand the aerodynamics and flow structures in the insect hovering flight, and the flying mechanisms relevant to the high lift production. However, the flow characteristics in this problem are certainly far more complex and diverse than the simple model considered here. Ideally, three-dimensional computation of the insect hovering flight is desirable and is a target in our further work.

Acknowledgments

This work was supported by the Innovation Project of the Chinese Academy of Sciences (Contract Nos. KJCX2-YW-L05 and CXJJ-237), the National Natural Science Foundation of China (Contract Nos. 10832010 and 10772173), and the Anhui Province Excellent Young Scholars Foundation (No. 08040106826).

References

[1] W. NACHTIGALL, Insects in Flight, Mchgraw-Hill, New York, 1974.
[2] A. K. BRODSKY, The Evolution of Insect Flight, Oxford University Press, Oxford, 1994.
[3] T. WEISH-FOGH AND M. JENSEN, *Biology and physics of locust flight. Basic principles of insect flight: a critical review*, Phil. Trans. Roy. Soc. Lond., 239 (1956), pp. 415.
[4] C. P. ELLINGTON, C. VAN DEN BERG, A. P. WILLMOTT AND A. L. R. THOMOS, *Leading-edge vortices in insect flight*, Nature, 384 (1996), pp. 626.
[5] J. M. BIRCH AND M. H. DICKINSON, *Spanwise flow and the attachment of the leading-edge vortex on insect wings*, Nature, 412 (2001), pp. 729.
[6] R. B. SRYGLEY AND A. L. R. THOMAS, *Unconventional lift-generating mechanisms in free-flying butterflies*, Nature, 420 (2002), pp. 660.
[7] L. A. MILLER AND C. S. PESKIN, *A computational fluid dynamics of 'clap and fling' in the smallest insects*, J. Exp. Biol., 208 (2005), pp. 195.
[8] T. WEIS-FOGH, *Quick estimates of flight fitness in hovering animals, including novel mechanism for lift production*, J. Exp. Biol., 59 (1973), pp. 169.
[9] R. J. COOTER AND P. S. BAKER, *Weis-Fogh clap and fling mechanism in* Locusta, Nature, 412 (1977), pp. 729.
[10] C. P. ELLINGTON, *The aerodynamics of insect flight III. Kinematics*, Phil. Trans. R. Soc. Lond. B., 305 (1984), pp. 41.
[11] J. H. MARDEN, *Maximum lift production during take-off in flying animals*, J. Exp. Biol., 130 (1987), pp. 235.
[12] A. R. ENNOS, *The kinematic and aerodynamics of the free flight of some* Diptera, J. Exp. Biol., 142 (1989), pp. 49.
[13] S. N. FRY, R. SAYAMAN AND M. H. DICKINSON, *The aerodynamics of free-flight maneuvers in* Drosophila, Science, 300 (2003), pp. 495.
[14] M. J. LIGHTHILL, *On the Weis-Fogh mechanism of lift generation*, J. Fluid Mech., 60 (1973), pp. 1.
[15] G. R. SPEDDING AND T. MAXWORTHY, *The generation of circulation and lift in a rigid two-dimensional fling*, J. Fluid Mech., 165 (1986), pp. 247.
[16] M. H. DICKINSON, F. O. LEHMANN AND S. P. SANE, *Wing rotation and the aerodynamic basis of insect flight*, Science, 284 (1999), pp. 1954.
[17] M. H. DICKINSON AND K. G. GÄTZ, *Unsteady aerodynamic performance of model wings at low Reynolds numbers*, J. Exp. Biol., 174 (1993), pp. 45.
[18] M. H. DICKINSON, *The effects of wing rotation on unsteady aerodynamic performance at low Reynolds number*, J. Exp. Biol., 192 (1994), pp. 179.
[19] S. P. SANE AND M. H. DICKINSON, *The control of flight force by a flapping wing: lift and drag production*, J. Exp. Biol., 204 (2001), pp. 2607.
[20] S. P. SANE AND M. H. DICKINSON, *The aerodynamic effects of wing rotation and a revised quasi-steady model of flapping flight*, J. Exp. Biol., 205 (2002), pp. 1087.
[21] F. O. LEHMANN, S. P. SANE AND M. H. DICKINSON, *The aerodynamic effects of wing-wing interaction in flapping inset wings*, J. Exp. Biol., 208 (2005), pp. 3075.
[22] R. J. BOMPHREY, N. J. LAWSON, G. K. TAYLOR AND A. L. R. THOMAS, *Application of digital particle image velocimetry to insect aerodynamics: measurement of the leading-edge vortex and near wake of a hawkmoth*, Exp. Fluids, 40 (2006), pp. 546.
[23] H. LIU AND K. KAWACHI, *A numerical study of insect flight*, J. Comput. Phys., 146 (1998), pp. 124.
[24] H. LIU, C. P. ELLINGTON, K. KAWACHI, C. VAN DEN BERG AND A. P. WILLMOTT, *A*

computational fluid dynamics study of hawkmoth hovering, J. Exp. Biol., 201 (1998), pp. 461.
[25] Z. J. WANG, *Two-dimensional mechanism of hovering*, Phys. Rev. Lett., 85 (2000), pp. 2216.
[26] Z. J. WANG, *The role of drag in insect hovering*, J. Exp. Biol., 207 (2004), pp. 4147.
[27] Z. J. WANG, J. M. BIRCH AND M. H. DICKINSON, *Unsteady forces and flows in low Reynolds number hovering flight: two-dimensional computations vs robotic wing experiments*, J. Exp. Biol., 207 (2004), pp. 449.
[28] M. SUN AND J. TANG, *Unsteady aerodynamic force generation by a model fruit fly wing in flapping motion*, J. Exp. Biol., 205 (2002), pp. 55.
[29] M. SUN AND S. L. LAN, *A computational study of the aerodynamic forces and power requirements of dragonfly (Aeschna juncea) hovering*, J. Exp. Biol., 207 (2004), pp. 1887.
[30] R. RAMAMURTI AND W. C. SANDBERG, *A three-dimensional computation study of the aerodynamic mechanisms of insect flight*, J. Exp. Biol., 205 (2002), pp. 1507.
[31] L. A. MILLER AND C. S. PESKIN, *A computational fluid dynamics of 'clap and fling' in the smallest insects*, J. Exp. Biol., 208 (2005), pp. 195.
[32] S. XU AND Z. J. WANG, *An immersed interface method for simulating the interaction of a fluid with moving boundaries*, J. Comput. Phys. **216**, 454 (2006).
[33] X. Y. LU AND Q. LIAO, *Dynamic responses of a two-dimensional flapping foil motion*, Phys. Fluids, 18 (2006), 098104.
[34] G. J. DONG AND X. Y. LU, *Characteristics of flow over traveling-wavy foils in a side-by-side arrangement*, Phys. Fluids, 19 (2007), 057107.
[35] M. H. SOHN AND J. W. CHANG, *Flow visualization and aerodynamic load calculation of three types of clap-fling motions in a Weis-Fogh mechanism*, Aerospace Sci. Tech., 11 (2007), pp. 119.
[36] F. M. BOS, D. LENTINK, B. W. VAN OUDHEUSDEN AND H. BIJL, *Influence of wing kinematics on aerodynamic performance in hovering insect flight*, J. Fluid Mech., 594 (2008), pp. 341.
[37] H. AONO1, F. Y. LIANG AND H. LIU, *Near- and far-field aerodynamics in insect hovering flight: an integrated computational study*, J. Exp. Biol., 211 (2008), pp. 239.
[38] G. LEWIN AND H. HAJ-HARIRI, *Modelling thrust generation of a two-dimensional heaving airfoil in a viscous flow*, J. Fluid Mech., 592 (2003), pp. 339.
[39] G. PEDRO, A. SULEMAN AND N. DJILALI, *A numerical study of the propulsive efficiency of a flapping hydrofoil*, Intl. J. Numer. Meth. Fluids., 42 (2003), pp. 1507.
[40] L. GUGLIELMINI AND P. BLONDEAUX, *Propulsive efficiency of oscillating foils*, Eur. J. Mech. B/Fluids., 23 (2004), pp. 255.
[41] F. HOVER, ϕ, HAUGSDAL AND M. TRIANTAFYLLOU, *Effect of angle of attack profiles in flapping foil propulsion*, J. Fluids Struc., 19 (2004), pp. 37.
[42] T. GAO AND X. Y. LU, *Insect normal hovering flight in ground effect*, Phys. Fluids., 20 (2008), 087101.
[43] M. BOUZIDI, M. FIRDAOUSS AND P. LALLEMAND, *Momentum transfer of a Boltzmann-lattice fluid with boundaries*, Phys. Fluids, 13 (2001), pp. 3452.
[44] P. LALLEMAND AND L. S. LUO, *Lattice Boltzmann method for moving boundaries*, J. Comput. Phys., 184 (2003), pp. 406.
[45] J. ZERIHAN AND X. ZHANG, *Aerodynamics of gurney flaps on a wing in ground effect*, AIAA J., 39 (2001), pp. 772.
[46] Y. MORYOSSEF AND Y. LEVY, *Effect of oscillations on airfoils in close proximity to the ground*, AIAA J., 42 (2004), pp. 1755.
[47] S. Y. CHEN AND G. D. DOOLEN, *Lattice Boltzmann method for fluid flows*, Annu. Rev. Fluid Mech., 30 (1998), pp. 329.
[48] Y. QIAN, D. D'HUMIERES AND P. LALLEMAND, *Lattice BGK models for Navier-Stokes equation*, Europhys. Lett., 17 (1992), pp. 479.

[49] D. YU, R. MEI AND W. SHYY, *A multi-block lattice Boltzmann method for viscous fluid flows*, Int. J. Numer. Method. Fluids., 39 (2002), pp. 99.
[50] Y. PENG, C. SHU, Y. T. CHEW, X. D. NIU AND X. Y. LU, *Application of multi-block approach in the immersed boundary-lattice Boltzmann method for viscous fluid flows*, J. Comput. Phys., 218 (2006), pp. 460.
[51] H. P. FANG, Z. W. WANG, Z. F. LIN AND M. R. LIU, *Lattice Boltzmann method for simulating the viscous flow in large distensible blood vessels*, Phys. Rev. E, 65 (2002), 051925.
[52] H. B. LI, X. Y. LU, H. P. FANG AND Y. H. QIAN, *Force evaluation in lattice Boltzmann simulations with moving boundaries in two dimensions*, Phys. Rev. E, 70 (2004), 026701-1.
H. P. FANG, Z. W. WANG, Z. F. LIN AND M. R. LIU, *Lattice Boltzmann method for simulating the viscous flow in large distensible blood vessels*, Phys. Rev. E, 65 (2002), 051925.
[53] J. Z. WU, Z. L. PAN AND X. Y. LU, *Unsteady fluid-dynamic force solely in terms of control-surface integral*, Phys. Fluids, 17 (2005), 098102.
[54] J. Z. WU, X. Y. LU AND L. X. ZHUANG, *Integral force acting on a body due to local flow structures*, J. Fluid Mech., 576 (2007), pp. 265.